

# Gas Diffusion, Energy Transport, and Thermal Accommodation in Single-Walled Carbon Nanotube Aerogels

Scott N. Schiffres, Kyu Hun Kim, Lin Hu, Alan J. H. McGaughey, Mohammad F. Islam, and Jonathan A. Malen\*

The thermal conductivity of gas-permeated single-walled carbon nanotube (SWCNT) aerogel (8 kg m<sup>-3</sup> density, 0.0061 volume fraction) is measured experimentally and modeled using mesoscale and atomistic simulations. Despite the high thermal conductivity of isolated SWCNTs, the thermal conductivity of the evacuated aerogel is 0.025 ± 0.010 W m<sup>-1</sup> K<sup>-1</sup> at a temperature of 300 K. This very low value is a result of the high porosity and the low interface thermal conductance at the tube–tube junctions (estimated as 12 pW K<sup>-1</sup>). Thermal conductivity measurements and analysis of the gas-permeated aerogel (H<sub>2</sub>, He, Ne, N<sub>2</sub>, and Ar) show that gas molecules transport energy over length scales hundreds of times larger than the diameters of the pores in the aerogel. It is hypothesized that inefficient energy exchange between gas molecules and SWCNTs gives the permeating molecules a memory of their prior collisions. Low gas-SWCNT accommodation coefficients predicted by molecular dynamics simulations support this hypothesis. Amplified energy transport length scales resulting from low gas accommodation are a general feature of CNT-based nanoporous materials.

## 1. Introduction

Thermally insulating and ultralight nanoporous materials or aerogels are attractive candidates for thermal/micrometeoroid insulation in weight-conscious applications such as satellites,<sup>[1]</sup> thermostatically controllable insulation, and heat pipes.<sup>[2]</sup> The most common types of thermally insulating foams with thermal conductivity,  $k$ , less than 0.01 W m<sup>-1</sup> K<sup>-1</sup> are silica, amorphous carbon, and polymeric aerogels.<sup>[3–5]</sup> These aerogels are typically electrical insulators. Recently, single-walled carbon nanotubes (SWCNTs) and multiwalled carbon nanotubes (MWCNTs) have been used to fabricate nanoporous materials,<sup>[6–8]</sup> primarily because carbon nanotubes (CNTs) have exceptional strength,

electrical conductivity, and thermal conductivity ( $k_{\text{MWCNT}} \approx 50\text{--}200$  W m<sup>-1</sup> K<sup>-1</sup>,  $k_{\text{SWCNT}} \approx 1000\text{--}3000$  W m<sup>-1</sup> K<sup>-1</sup>).<sup>[9–14]</sup> The CNTs in these nanoporous materials interact through van der Waals interactions between CNTs. Compared to other aerogels, CNT-based nanoporous materials possess high electrical conductivity and high specific surface area, and will be useful in super-capacitors, desalination membranes, lithium-air battery electrodes, permeable catalysis scaffolding, gas sensors, and thermoelectric devices.<sup>[15–24]</sup>

Inter-nanoparticle bonding and nanoparticle defectiveness are reported to impact electrical conductivities of carbon-based nanoporous materials, and similar trends are emerging for thermal properties.<sup>[6–8,25]</sup> For example, the thermal conductivities of carbon-based nanoporous materials in the form of graphene foams (10–12 kg m<sup>-3</sup>, few-layer graphene), vertically-aligned arrays (41 kg m<sup>-3</sup>, SWCNTs), sponges (7.5 kg m<sup>-3</sup>, MWCNTs), and mats (390 kg m<sup>-3</sup>, SWCNTs & MWCNTs) have been reported as 0.26–1.70 W m<sup>-1</sup> K<sup>-1</sup>,<sup>[25]</sup> 0.55 W m<sup>-1</sup> K<sup>-1</sup>,<sup>[6,26]</sup> 0.15 W m<sup>-1</sup> K<sup>-1</sup>,<sup>[7,8]</sup> and 0.16 W m<sup>-1</sup> K<sup>-1</sup>.<sup>[27]</sup> Despite the extremely high thermal conductivity of individual SWCNTs and graphene molecules, in excess of 1000 W m<sup>-1</sup> K<sup>-1</sup>,<sup>[10–14,28]</sup> large thermal boundary resistance at nanoparticle-nanoparticle junctions drastically lowers the thermal conductivity of carbon-based nanoporous materials.<sup>[27]</sup> Environment-dependent studies of thermal transport have been performed on isolated CNT bundles to identify gas-CNT heat transfer coefficients,<sup>[29,30]</sup> yet not in CNT networks. Technologically important knowledge gaps, such as the effect of the CNT accommodation coefficient on gas diffusion through the nanoporous network, remain unresolved.

Here, we report on the efficiency of phonon transport through a van der Waals bonded SWCNT aerogel, the nature of gas diffusion in the aerogel, and the efficiency of energy exchange between gas molecules and the SWCNTs using pressure-dependent thermal conductivity measurements and multiscale simulations. SWCNT aerogels are fabricated from solution-processed and purified SWCNTs,<sup>[31,32]</sup> in contrast to other CNT-based nanoporous materials,<sup>[6–8]</sup> which may contain residual impurities from chemical vapor deposition-based synthesis approaches. We measured the thermal conductivity of two SWCNT aerogels (8 kg m<sup>-3</sup>, volume fraction  $\phi_{\text{SWCNT}} = 0.0061$ )<sup>[33]</sup> in five different permeating gases (H<sub>2</sub>, He, Ne, N<sub>2</sub>,

S. N. Schiffres, Dr. L. Hu, Prof. A. J. H. McGaughey,  
Prof. J. A. Malen  
Department of Mechanical Engineering  
Carnegie Mellon University  
5000 Forbes Ave., Pittsburgh, PA 15213  
E-mail: jonmalen@andrew.cmu.edu  
K. H. Kim, Prof. M. F. Islam, Prof. J. A. Malen  
Department of Materials Science & Engineering  
Carnegie Mellon University  
5000 Forbes Ave., Pittsburgh, PA 15213



DOI: 10.1002/adfm.201201285

and Ar) from low (0.1 kPa) to atmospheric (101 kPa) pressure. Our results suggest that the thermal resistance at junctions formed by van der Waals interactions between SWCNTs negates the high thermal conductivity of each SWCNT and allows us to estimate the thermal resistance between SWCNTs. Further, we infer from our measurements that the ballistic travel distance of a gas molecule between collisions with the SWCNTs within the aerogel is two orders of magnitude greater than the characteristic aerogel pore size. We propose that this drastic length-scale difference is due to the open-cell network and the inefficient energy exchange between gas molecules and SWCNTs, which lengthens the mean distance energy is transported. Molecular dynamics (MD) and mesoscale simulations support our hypothesis, and clarify that this is a general feature of CNT-based nanoporous materials.

## 2. Results and Discussion

### 2.1. SWCNT Aerogel Characterization

The SWCNT aerogels were synthesized from an aqueous SWCNT solution (diameter:  $0.9 \pm 0.2$  nm, length: 300 nm to 2.3  $\mu\text{m}$ ) in a vessel customized for thermal conductivity measurements. Details about the SWCNT aerogel fabrication are provided in the Methods section.

The porous network of SWCNTs was imaged using scanning electron microscopy (SEM) (FEI Quanta 600) and transmission electron microscopy (TEM) (FEI Tecnai F20) to verify that the SWCNTs were well-dispersed. High resolution SEM images of cross-sections of SWCNT aerogel show an isotropic porous network of individual SWCNTs with an open-cell-like structure (Figure 1a), which was further confirmed by low-resolution TEM imaging (Figure 1b). The SWCNT aerogel specific surface area and pore size distribution were determined using the Brunauer-Emmett-Teller (BET) surface area measurement method and nitrogen adsorption.<sup>[34]</sup> The BET measurements indicated that the aerogels have mesopores (diameters in the range of 2-50 nm), with few micropores (diameters less than 2 nm) and few macropores (diameters greater than 50 nm) (Figure S1a,b, Supporting Information).<sup>[34]</sup> The measured specific surface area of the aerogel was  $1190 \text{ m}^2 \text{ g}^{-1}$ ,<sup>[35]</sup> which is close to the theoretical limit for SWCNTs of  $1315 \text{ m}^2 \text{ g}^{-1}$ ,<sup>[36]</sup> further confirming that the SWCNTs were isolated and unbundled within the aerogel.

Thermal conductivity measurements were performed on the SWCNT aerogel using a modified  $3\omega$  method developed specifically for low-thermal conductivity materials.<sup>[37]</sup> This technique, which is called metal-coated  $3\omega$ , is capable of measuring small samples with reduced sensitivity to conduction and radiation losses at the sample boundaries, as compared to steady-state techniques like guarded hot-plate.<sup>[37]</sup> The measurements were performed in vessels with a  $15 \times 10 \times 5 \text{ mm}^3$  cavity spanned

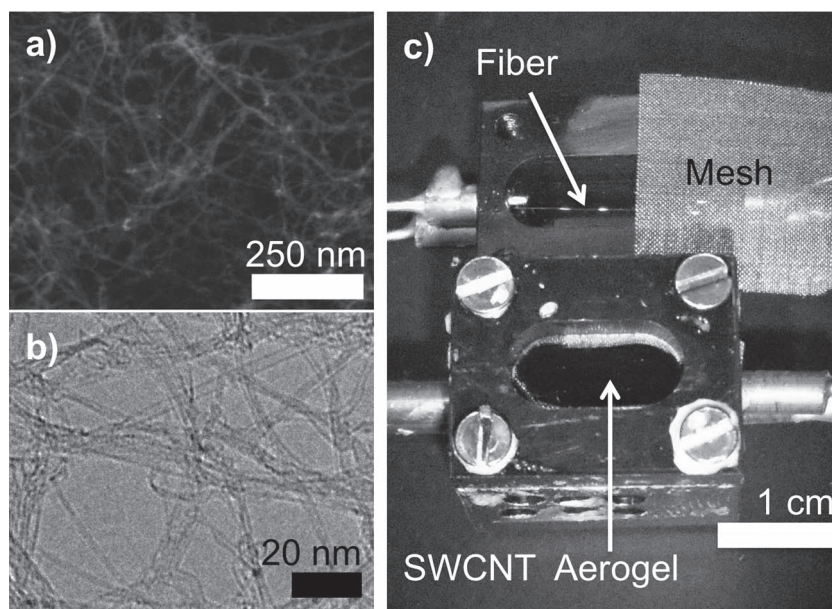


**Figure 1.** Images of SWCNT aerogels and custom vessel for thermal conductivity measurements. a) SEM cross-sectional image showing the SWCNT network. Readily discernible SWCNT struts confirm that the SWCNTs are well dispersed in the aerogel structure. b) Low-resolution TEM image shows that the network is composed of mostly isolated and entangled SWCNTs. c) Top: samples are formed in a holder with a suspended gold coated fiber that is used as a thermal conductivity probe. The fine mesh holds the elastic gel in place during synthesis, allowing for solvent exchange and critical point drying of the aerogel. Bottom: this SWCNT aerogel sample was used for thermal conductivity measurements (Sample 2).

by a suspended Au coated (100 nm thick) glass fiber (25  $\mu\text{m}$  in diameter). An empty vessel, prior to aerogel synthesis, is shown in the top of Figure 1c. Using the synthesis process described in the Methods section, the SWCNT elastic gel was formed around this suspended fiber. A fine mesh held the elastic gel in the cavity, while allowing for solvent removal and critical point drying. A vessel with an aerogel sample inside is pictured in the bottom of Figure 1c.

To measure thermal conductivity, the Au coated glass fiber acts simultaneously as a resistance-based heater and thermometer. A periodic current  $I$  at a frequency  $1\omega$  is driven through the Au coating, causing Joule heating at a frequency  $2\omega$ . This heating results in a periodic temperature change in the Au coating, having an amplitude related to the thermal conductivity of the surrounding SWCNT aerogel. Small changes in the Au temperature induce an electrical resistance change, as quantified by the coefficient of thermoresistance  $[\beta = (1/R) dR/dT]$ , where  $R$  is the electrical resistance and  $T$  is the temperature.  $\beta$  was determined independently by measuring the  $dR/dT$  of the Au coating when the sample temperature was swept in an oven. Through thermoresistance, the periodic temperature oscillation induces a periodic electrical resistance oscillation in the Au coating at a frequency  $2\omega$ . The voltage measured across the Au coating then has a  $3\omega$  component due to the Ohm's law multiplication of the  $2\omega$  resistance with the  $1\omega$  current. This  $3\omega$  signal is measured with a lock-in amplifier. Periodic heating naturally confines the thermal response to a penetration depth  $L_p = \sqrt{\alpha/\omega}$  into the aerogel, where  $\alpha$  is its thermal diffusivity ( $k/c_p$ , where  $c_p$  is the volumetric specific heat at constant

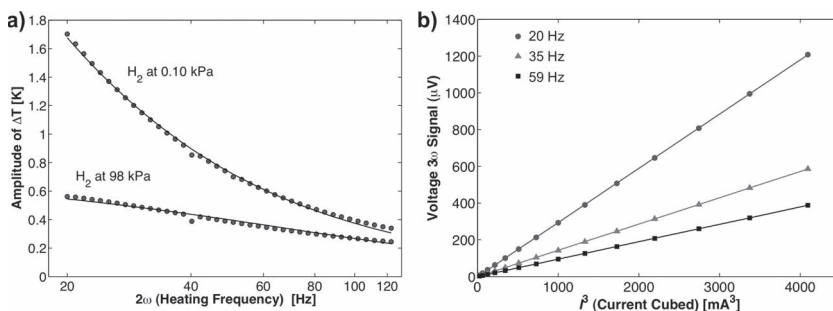


**Figure 2.** Thermal conductivity measurement data analysis and validation. a) Representative  $3\omega$  amplitude versus frequency data and fits to thermal conductivity. Data shown for sample 1 in  $H_2$  at pressures of 0.10 kPa and 98 kPa. b) The  $3\omega$  voltage signal plotted versus current shows the expected cubed power law (cubic best fits shown as solid lines). This validation was performed in He at atmospheric pressure with  $1\omega$  current source frequencies of 20, 35, and 59 Hz.

pressure). Our measured values of  $k$ , described next, result in  $100 \mu\text{m} < L_p < 1000 \mu\text{m}$ , which ensures that the aerogel samples appear semi-infinite to the temperature response and are insensitive to external boundary conditions.

The thermal conductivity of the sample was determined by fitting the temperature amplitude inferred from the  $3\omega$  signal, as a function of the applied frequency, to an analytical heat conduction model described previously.<sup>[37]</sup> Representative fits are shown in **Figure 2a** for aerogel sample 1 in  $H_2$  at pressures of 0.10 kPa and 98 kPa. The thermal conductivity of the aerogel at each measurement condition was found using a least squares fit with thermal conductivity as the sole fitting parameter. Reference values for graphite specific heat were used as the SWCNT specific heat.<sup>[38]</sup> The  $3\omega$  amplitude has the expected linearly increasing relationship with  $I^3$ , as shown in **Figure 2b**, verifying that our results are not influenced by parasitic conduction through the aerogel or extrinsic non-linearities.<sup>[39]</sup>

The thermal conductivities of the SWCNT aerogel versus pressure with  $H_2$ , He, Ne,  $N_2$ , and Ar filling gases at temperature of 300 K are plotted in **Figure 3** for sample 1 (the solid line fits are discussed later). Data and fits for sample 2 are included in the Supporting Information. At pressures below 150 Pa, the thermal conductivity converges to  $0.025 \pm 0.010 \text{ W m}^{-1} \text{ K}^{-1}$  (the average of two samples), independent of the permeating gas. This 95% confidence interval of the extracted thermal conductivity was calculated by assessing the thermal conductivity variation due to uncertainty in the input parameters, including fiber length, fiber diameter, aerogel heat capacity, and  $\beta$ . The evacuated thermal conductivity value, further referred to as  $k_{\text{evacuated}}$ , includes the effects of solid conduction through the SWCNT network and radiation exchange between SWCNTs, which are both independent of gas pressure. The total thermal conductivity,  $k_{\text{total}}$ , at higher pressures is the sum of  $k_{\text{evacuated}}$  and the gas contribution to thermal conductivity  $k_{\text{gas}}$ .<sup>[40]</sup>

$$k_{\text{total}} = k_{\text{evacuated}} + k_{\text{gas}} \quad (1)$$

Within the measurement uncertainty,  $k_{\text{gas}}$  reaches the bulk gas thermal conductivity by atmospheric pressure except for  $H_2$ . Reference values for the thermal conductivities of  $H_2$ , He, Ne,  $N_2$ , and Ar (0.182, 0.155, 0.0483, 0.0260, and  $0.0177 \text{ W m}^{-1} \text{ K}^{-1}$ )<sup>[41–43]</sup> plus the SWCNT aerogel's evacuated

thermal conductivities are marked on **Figure 3**. Equation 1 may have been violated in the  $H_2$  environment because an adsorbed  $H_2$  layer enhances the thermal conductance between SWCNTs or because of sourcing/sinking of heat due to adsorption/desorption of  $H_2$  during the experiment.<sup>[44–47]</sup>

Among other studied CNT materials (vertically-aligned CNT arrays, CNT sponges, and CNT mats), the SWCNT aerogel has the lowest thermal conductivity, but its thermal diffusivity fits in the middle of these materials ( $4.2 \times 10^{-6} \text{ m}^2 \text{ s}^{-1}$ ). The SWCNT aerogel thermal diffusivity is five times smaller than that of the denser vertically aligned CNT arrays<sup>[6,26]</sup> and seven times smaller than that of the comparably-light CNT sponges.<sup>[7,8]</sup>

Compressed mats of CNTs<sup>[27]</sup> have about six times lower thermal diffusivity than the SWCNT aerogel. Like the SWCNT aerogel, the tube-tube junctions of the compressed mats are van der Waals bonded, but the tangling and inter-nanoparticle contact maybe poorer than solution formed aerogels. nanoporous graphitic foams with covalently bonded nanoparticles have thermal diffusivities that are more than ten times larger than the SWCNT aerogel. Similar trends for mechanical and electrical conductivity have been observed in graphitic nanoporous materials.<sup>[48,49]</sup>

## 2.2. Phonon Transport through the SWCNT Aerogel

SWCNTs possess extremely high thermal conductivity as single molecules (in excess of  $1000 \text{ W m}^{-1} \text{ K}^{-1}$ ),<sup>[10–14]</sup> yet the thermal

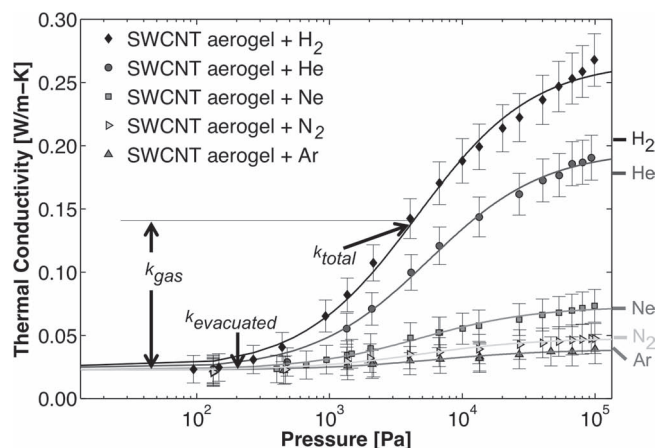


**Figure 3.** Plot of effective total thermal conductivity for sample 1 versus gas pressure. The gas contribution to thermal conductivity  $k_{\text{gas}}$  of  $H_2$  at 4 kPa is illustrated as the difference between the aerogel's total thermal conductivity  $k_{\text{total}}$  in  $H_2$  at 4 kPa and the evacuated thermal conductivity  $k_{\text{evacuated}}$ . Fits to Equation 5 from kinetic theory are shown as solid lines for each gas. The kinetic theory model fits two free variables for each gas, the cross-sectional collision diameter  $\sigma$  and structural free path  $r_e$ . The reported error bars are due to propagated uncertainty in fiber length, fiber diameter, and coefficient of thermal resistance  $\beta$  (see text). The tick marks to the right of the plot indicate the expected atmospheric  $k_{\text{evacuated}} + k_{\text{gas}}$ .

conductivities of CNT-based materials are far lower due to thermal resistance at tube-tube junctions. The thermal conductance of the tube-tube junctions was estimated from  $k_{\text{evacuated}}$  through the application of effective medium theory (see Experimental Section). From this analysis, the thermal conductance between SWCNTs,  $h$ , is  $12_{-6}^{+13}$  pW K<sup>-1</sup>. While no direct measurements of  $h$  between SWCNTs are available for comparison, Yang et al.<sup>[9]</sup> measured a junction conductance of 21 pW K<sup>-1</sup> for multi-walled CNTs (diameter 1.4 nm) with perpendicular junctions. If these measurements are rescaled for a diameter of 0.9 nm using a proposed diameter-squared scaling law,<sup>[9]</sup> the predicted junction conductance is 9 pW K<sup>-1</sup>. Prasher et al. experimentally found a junction conductance of 3 pW K<sup>-1</sup> for SWCNTs in a compressed mat, but found that atomistic simulations yield much higher values ( $\approx 50$  pW K<sup>-1</sup>).<sup>[27]</sup> Agreement between  $h$  of the SWCNT and prior measurements is of the same order. It is noteworthy that the thermal resistance due to  $h$  is more than 100 times greater than that due to conduction through the SWCNTs. This result confirms that the excellent phonon transport properties of SWCNTs can be overshadowed by poor tube-tube phonon conductance in the SWCNT network.

### 2.3. Gas Transport and Energy Exchange in SWCNT Aerogel

Kinetic theory and multiscale simulations are now used to understand how  $k_{\text{gas}}$  depends on pressure. The kinetic theory expression for gas thermal conductivity is

$$k = \frac{c_v v l \varepsilon}{3} \quad (2)$$

where  $c_v$  is the volumetric specific heat,  $v$  is the gas root mean squared (RMS) velocity,  $l$  is the gas molecule mean free path (i.e., the average distance a gas molecule travels before a scattering event), and  $\varepsilon$  is the correction factor between the kinetic theory expressions for viscosity and thermal conductivity (2.50 for noble gases, 1.47 for H<sub>2</sub>, and 1.95 for N<sub>2</sub>).<sup>[50]</sup> The kinetic theory expression for the bulk mean free path is

$$l_{\text{bulk}} = \frac{k_B T}{\sqrt{2} P \sigma^2} \quad (3)$$

where  $\sigma$  is the collision diameter of the gas molecule,  $P$  is pressure,  $T$  is temperature, and  $k_B$  is the Boltzmann constant.<sup>[50]</sup> In a bulk gas, thermal conductivity is independent of pressure because the volumetric specific heat is proportional to pressure (i.e., it is proportional to the number density of molecules), while the mean free path is inversely proportional to pressure. As pressure is reduced in the aerogel, however, gas-gas collisions become less frequent and gas-SWCNT collisions become more frequent. In the limit of very low pressures, energy carried by the permeating gas will travel an energy mean free path,  $r_e$ .

The gas mean free path in the transition region between the gas having primarily gas-SWCNT collisions (low-pressure) and the gas having primarily gas-gas collisions (high-pressure) can

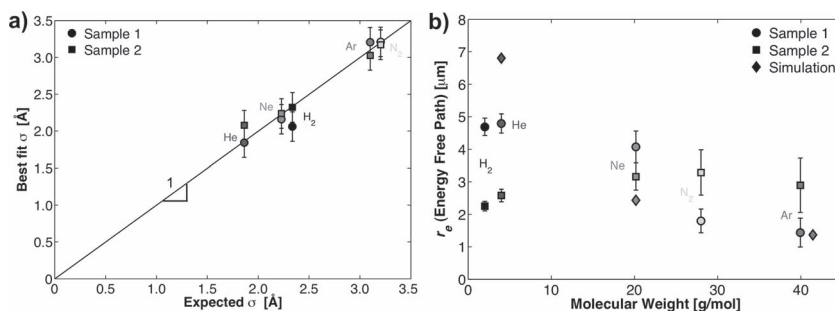


**Figure 4.** Kinetic theory fits of thermal conductivity versus pressure yield two variables: collision diameter  $\sigma$  and mean free path  $r_e$ . a) Plot of kinetic theory fit  $\sigma$  versus expected values of  $\sigma$ . b) Kinetic theory  $r_e$  for H<sub>2</sub>, He, Ne, N<sub>2</sub>, and Ar and simulated  $r_s/\alpha$  versus gas molecular weights for He, Ne, and Ar. The simulated Ar  $r_e$  data point has been offset in molecular weight to aid viewing.

be described by an effective mean free path,  $l_E$ , which can be estimated using the Mattiesson rule to be<sup>[51]</sup>

$$\frac{1}{l_E} = \frac{1}{l_{\text{bulk}}} + \frac{1}{r_e} \quad (4)$$

Substituting Equation 3 into Equation 4 and setting  $l$  in Equation 2 equal to  $l_E$  gives an expression for the gas thermal conductivity as a function of  $P$ ,  $\sigma$ , and  $r_e$ :

$$k = \frac{c_v v \varepsilon}{3} \left( \frac{\sqrt{2} P \sigma^2}{k_B T} + \frac{1}{r_e} \right)^{-1} \quad (5)$$

Values of  $\sigma$  and  $r_e$  were determined by fitting the gas contribution to thermal conductivity as a function of  $P$  using Equation 5. The RMS velocity is  $\sqrt{3k_B T/m}$ , where  $m$  is the molecular weight of the gas molecule. The fits capture the experimental trends for all five gases, as shown in Figure 3. As shown in Figure 4a, the fit values of  $\sigma$  for both samples closely match those predicted from NIST bulk gas viscosity data using the kinetic theory expression for viscosity ( $\rho v l/3$ , where  $\rho$  is density).<sup>[50]</sup> The fit values of  $r_e$  for both samples are plotted in Figure 4b. Values ranging from 1-5  $\mu\text{m}$  were found in both samples. The trend in the  $r_e$  values for sample 1 is to decrease with increasing gas molecular weight, while the trend for sample 2 is relatively flat with molecular weight.

The measured  $r_e$  values are significantly larger than the pores (2–50 nm) in the aerogel. To understand the origin of this discrepancy, we simulated gas transport through the SWCNT aerogel. As shown in Figure 5, the mesoscale simulation ( $1.05 \times 1.05 \times 1.05 \mu\text{m}^3$ , periodic boundary conditions) is a random network of SWCNTs modeled as chain of beads with a density of 8 kg m<sup>-3</sup> (see Experimental Section). A gas molecule randomly placed on a SWCNT is moved along a randomly chosen direction until colliding with another SWCNT. A collision is said to occur when the distance from the gas molecule to a bead is less than sum of the SWCNT radius and the gas molecule radius. This procedure was repeated ten thousand times and the collision distances follow a Poisson distribution. The average distance, referred to as the structural mean free path,  $r_s$ , ranged from 375 nm (argon) to 450 nm (helium), with less than 1% variation between sample sets. These structural mean free paths are much larger than the pore diameter (2–50 nm),

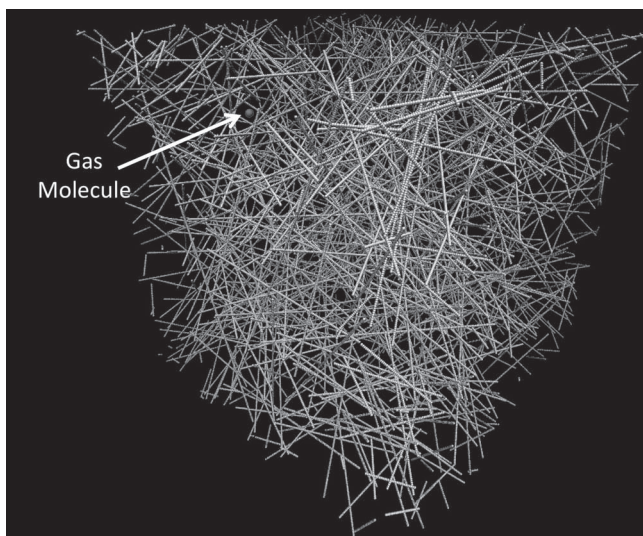


**Figure 5.** To predict the structural mean free path of a gas molecule in the SWCNT aerogel, a 3D network model was created. The mesoscale model is  $1.05 \times 1.05 \times 1.05 \mu\text{m}^3$  with periodic boundary conditions (a  $300 \times 300 \times 300 \text{ nm}^3$  sub-section is shown). The SWCNTs are represented by a string of beads and are each  $1 \mu\text{m}$  long. A gas molecule was randomly placed in the model (i.e., the sphere) and moved along a randomly chosen direction until a collision with a SWCNT occurred. This process was repeated 10 000 times and the free paths were averaged to extract the structural mean free path.

because the pores are open-celled, yet are still far smaller than the  $r_e$  values.

We hypothesize that inefficient energy exchange between gas molecules and SWCNTs causes the order-of-magnitude difference between the energy mean free path,  $r_e$ , obtained by fitting the  $k_{\text{gas}}$  data to kinetic theory, and the structural mean free path,  $r_s$ , found from simulating gas movement through the aerogel. The kinetic theory-based  $r_e$  wrongly assumes that the gas molecules' average temperature after a collision with the SWCNT is that of the SWCNT. Instead, the extent of thermal acclimation is characterized by the energy accommodation coefficient, defined as  $\alpha = \frac{(E_{\text{in}} - E_{\text{re}})}{(E_{\text{in}} - E_{\text{W}})}$ , where  $E_{\text{in}}$  and  $E_{\text{re}}$  represent the energy fluxes incident to and reflected from the SWCNT and  $E_{\text{W}}$  is the energy that would be leaving the SWCNT if the reflected gas molecules had a distribution of energy characteristic of the wall temperature.<sup>[50,52]</sup>

To test this hypothesis, MD simulations were performed to estimate the accommodation coefficient of the noble gases (He, Ar, Ne) with a SWCNT. The MD simulation we designed tracks the average energy change of a gas molecular stream interacting with a SWCNT (see the Experimental Section for details and the simulation cell shown in **Figure 6**). The calculated energy accommodation coefficients are  $0.07 \pm 0.01$  for helium,  $0.16 \pm 0.03$  for neon, and  $0.30 \pm 0.10$  for argon. These values are all much less than one, confirming poor energy exchange during collisions.

We now seek a relationship between  $r_e$ ,  $r_s$  and  $\alpha$  to confirm that inefficient energy exchange causes the discrepancy between  $r_e$  and  $r_s$ . Consider a gas molecule stream that has multiple collisions with a SWCNT structure at  $T_{\text{SWCNT}}$ . The gas molecule

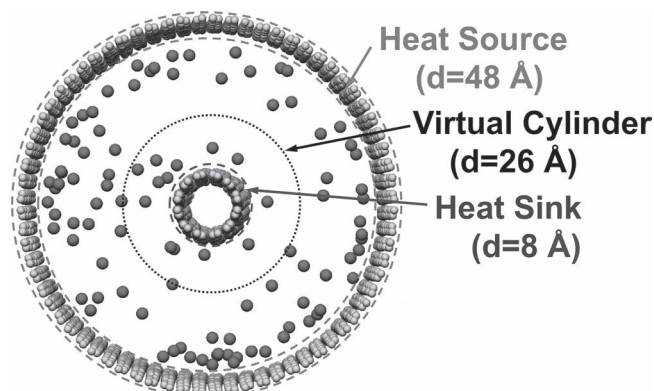


**Figure 6.** The MD simulation model used to predict the energy accommodation of various gases with SWCNTs is pictured. The simulation consists of two concentric SWCNTs, with energy being sourced to the outer SWCNT and sunk from the inner SWCNT. The thermal accommodation coefficient was calculated by tracking the energy of gas molecules (the spheres) passing through the virtual cylinder (positioned one cutoff length away from the inner SWCNT).

stream reaches a temperature  $T_i$  after the  $i^{\text{th}}$  gas-SWCNT collision. The gas molecule stream temperature after the next gas-SWCNT collision is

$$T_{i+1} = \alpha (T_{\text{SWCNT}} - T_i) + T_i \quad (6)$$

The temperature difference through a gas-SWCNT collision,

$$T_{i+1} - T_i = \alpha (T_{\text{SWCNT}} - T_i) \quad (7)$$

is proportional to the energy transferred in the collision, as the energy transferred is the product of the temperature difference and specific heat. This collision transports a fraction  $\alpha$  of the energy a distance  $r_s$  (the structural free path). The remaining fraction of incoming gas energy,  $1 - \alpha$ , will from that point (already having traveled  $r_s$ ) travel a distance  $r_e$  further such that

$$r_e = \alpha r_s + (1 - \alpha) (r_s + r_e) \quad (8)$$

which can be rearranged to give

$$\frac{r_e}{r_s} = \frac{1}{\alpha} \quad (9)$$

This relation shows that in the low-pressure limit (i.e., when the bulk gas mean free paths are much longer than the pore size), the thermal energy is transported  $r_e$ , a longer distance than  $r_s$ , due to sub-unity gas-SWCNT accommodation. Physically, the lower the gas-SWCNT thermal accommodation, the longer the thermal memory of the gas molecules. An alternative derivation of Equation 9 is shown in the Supporting Information.

The quotients of  $r_s$  and  $\alpha$  obtained from the modeling work are plotted for the noble gases in Figure 4b, for comparison with the experimental values of  $r_e$ . The measured values of  $r_e$  for sample 1 and 2 agree in magnitude to these simulated values of  $r_e$ . Additionally, there is rough agreement in the trend of the measured  $r_e$  for sample 1 and the simulated  $r_s/\alpha$ . Although the magnitudes of the  $r_e$  values from sample 2 are consistent with the simulation, there is less variation in measured  $r_e$  between the gases and no strong trend of decreasing accommodation with increasing gas molecular weight. This discrepancy may be

caused by sample 2's longer exposure to a non-inert gas environment, as surface contamination can drastically change the thermal accommodation properties.<sup>[52,53]</sup> Repeated experiments following one week of high-vacuum containment on sample 2 yielded identical results within experimental uncertainty.

The trend of decreasing  $r_c$  seen in Figure 4b for sample 1 and the simulated  $r_s/\alpha$  stems from improved accommodation of heavier gas molecules. This trend agrees with the relative ratio of accommodation coefficients for various gases with SWCNTs measured by Hsu et al.<sup>[29]</sup> Accommodation coefficients generally increase with increasing gas molecular weight because heavier gas molecules penetrate deeper into the wall's intermolecular potential.<sup>[53]</sup>

### 3. Conclusions

Our study of the thermal conductivity of SWCNT aerogel yields novel insight into phonon transport through SWCNT junctions, gas diffusion through SWCNT aerogels, and thermal accommodation of various gases with SWCNTs. Our thermal conductivity-based approach to understanding gas diffusion and energy exchange in the aerogel identified a length scale for energy transport over two orders of magnitude larger than the pore size. We reconciled this difference through the low gas-SWCNT thermal accommodation coefficient and the open-cell network structure of the SWCNT aerogel. This understanding will guide material scientists and application engineers who want to harness the unique thermal and gas-diffusion properties of SWCNT aerogels and related nanoporous materials in diverse applications.

### 4. Experimental Section

**SWCNT Aerogel Fabrication:** SG76 SWCNTs (diameter:  $0.9 \pm 0.2$  nm, length: 300 nm to 2.3  $\mu\text{m}$ ) produced by the CoMoCAT method were obtained from SouthWest NanoTechnologies Inc. and purified as previously reported prior to the actual use for synthesis in order to remove any residual metal catalyst and carbonaceous impurities.<sup>[54]</sup> Purified SWCNTs were suspended in deionized water (Millipore) using sodium dodecylbenzene sulfonate (SDBS) surfactant (Acros Organics) at a SWCNT dispersion concentration of  $1 \text{ kg m}^{-3}$ ; the mass ratio of SWCNT:SDBS was 1:10.<sup>[31,32,54,55]</sup> The solution was then tip-sonicated (Thermo Fisher 500) for 2 h at 60 W; the temperatures of the dispersions were maintained at room temperature during sonication using a large water bath. The SWCNT dispersions were centrifuged at 21 000 g for 30 min (Beckman Coulter Allegra 25R) to sediment SWCNT bundles. The supernatant was collected to fabricate SWCNT aerogels. The SWCNT concentration in the supernatant was determined using optical absorbance spectra (Varian Cary 5000 visible-near infrared spectrometer) with an extinction coefficient of 2.6 (absorbance mL)/(mg mm) at 930 nm and the Lambert-Beer equation.<sup>[56]</sup> The average SWCNT concentration in the supernatant was higher than  $0.75 \text{ kg m}^{-3}$ . The absorption spectra from the supernatant showed sharp van Hove peaks, confirming SWCNTs were left intact after our purification and dispersion processes.<sup>[21,22]</sup> The supernatant was then ultracentrifuged at 51 000 rpm (270 000 g) for 5 h (Beckman Coulter L-100K, rotor type 70Ti) to sediment SWCNTs. The sedimented SWCNTs were collected and redispersed in water at a concentration of  $\approx 2.5 \text{ kg m}^{-3}$  using a SDBS solution of concentration  $5 \text{ kg m}^{-3}$  and then tip sonicated for 10 to 20 min. The solution was then further concentrated by evaporating water off to a final concentration of 3.3 to 3.7  $\text{kg m}^{-3}$ . Bubbles generated

due to cavitation during the sonication were removed by degassing the concentrated SWCNT solution in vacuum and then poured the solution into the custom vessels containing the Au-coated optical fiber. To avoid further drying, the SWCNT solution was left sealed up with parafilms, and it formed a hydrogel within  $\approx 12$  h.<sup>[31,32,57]</sup> After complete gelation of the solution, we removed the residual SDBS surfactant in the hydrogel by soaking the gel in water first for 3 h. Water was exchanged with ethanol by sequentially soaking the hydrogel in different concentrations of ethanol varying from 20–100% with the step size of 20% for 24 h under ambient lab conditions. Ethanol enhanced the removal of the surfactant, but direct soaking in high concentration of ethanol resulted in significant shrinkage. High temperature processes were avoided in order not to damage the thermal conductivity measurement fiber. The sample was dried in a critical-point-dryer (CPD; Tousimis Autosamdri-815) after exchanging ethanol with liquid carbon dioxide ( $\text{LCO}_2$ ) and created a SWCNT aerogel. The aerogel density was estimated by measuring the volume and mass of aerogels made by the same technique. TEM imaging of a cross-section of SWCNT aerogels (Figure 1b) showed minimal residual surfactant and SWCNT walls were clearly visible. Energy dispersive X-ray spectroscopy (EDX) analysis showed  $<1$  wt% of sodium and sulfur, which are components of the surfactant, in SWCNT aerogel (Figure S3, Supporting Information), further indicating that the aerogels were essentially surfactant-free;<sup>[31]</sup> note, quantitative analysis limit of EDX was below 1 wt%. Aqueous dispersions created from powdered SWCNT aerogels clearly showed van Hove peaks in NIR fluorescence spectra (Figure S2a, Supporting Information) similar to the spectra obtained from SWCNT suspensions before hydrogel formation, confirming that SWCNTs remained well-preserved through the aerogel fabrication process. The radial breathing modes (RBM) and the peak intensity ratio of D-band to G-band were similar for nanotube powder prior to any processing and aerogels (Figure S2b, Supporting Information), also indicating structural integrity of nanotubes in the aerogels.

**Junction Thermal Conductance Estimation:** The effective medium theory thermal conductivity expression for a network of perfectly contacting randomly oriented tubes is  $k_{\text{effective}} = k_{\text{tube}}\phi_{\text{tube}}/3$ ,<sup>[27,58]</sup> where  $k_{\text{tube}}$  is the tube thermal conductivity,  $\phi_{\text{tube}}$  is the tube volume fraction, and the factor of three accounts for the random orientation of the tubes. This expression is applied to evaluate the effective SWCNT thermal conductivity,  $k_{\text{ESWCNT}}$ , by substituting  $\phi_{\text{SWCNT}}$  for  $\phi_{\text{tube}}$ ,  $k_{\text{ESWCNT}}$  for  $k_{\text{tube}}$ , and  $k_{\text{evacuated}}$  for  $k_{\text{effective}}$ . This yields  $k_{\text{ESWCNT}} = 12 \pm 5 \text{ W m}^{-1} \text{ K}^{-1}$  for  $\phi_{\text{SWCNT}} = 0.0061$ , which is two orders-of-magnitude lower than measurements of individual SWCNT thermal conductivity.<sup>[10–14]</sup> This discrepancy stems from the finite thermal conductance at the tube-tube junctions,  $h$ . By writing the effective thermal resistance,  $R_{\text{total}}$ , as the sum of the resistance due to thermal transport along the tube,  $R_{\text{tube}}$ , and the resistance due to thermal transport through the tube-tube junction,  $R_{\text{junction}}$ , the tube-tube conductance can be estimated. The total thermal resistance to energy transport is  $R_{\text{total}} = L/k_{\text{ESWCNT}}A$ , where  $L$  is the tube length and  $A$  is the tube cross-sectional area. Similarly, the thermal resistance imposed by conduction along a tube is  $R_{\text{tube}} = L/k_{\text{SWCNT}}A$ , where the literature value of  $k_{\text{SWCNT}} = 3000 \text{ W m}^{-1} \text{ K}^{-1}$ <sup>[10–14]</sup> is used. The thermal resistance from the tube-tube junctions is  $R_{\text{junction}} = 1/h$ . These expressions are related as  $R_{\text{total}} = R_{\text{tube}} + R_{\text{junction}}$  to find  $h$  from

$$\frac{L}{k_{\text{ESWCNT}}A} = \frac{L}{k_{\text{SWCNT}}A} + \frac{1}{h} \quad (10)$$

From this expression,  $h$  is  $12^{+13}_{-6} \text{ pW K}^{-1}$ , assuming  $A = 2\pi r\delta$  and  $L = 1.0 \pm 0.5 \mu\text{m}$  (the average length of the SWCNTs), where  $r$  is the radius of the SWCNTs and  $\delta$  is the layer separation in graphite (0.335 nm). This model is meant to provide an order of magnitude estimate of the thermal boundary conductance and assumes that van der Waal bonds to other SWCNTs do not significantly decrease the thermal conductivity within an SWCNT and that each SWCNT transports thermal energy its full length.

**Structural Free Path Simulation:** To estimate the mean free path of the gas molecules in the SWCNT aerogel in the absence of gas-gas collisions, a model representing the structure of the SWCNT aerogel was constructed. To allow for simulation of large enough systems, the

SWCNT structure was simplified using beads, with one bead per 0.5 nm of SWCNT. The beads on the same SWCNT are connected by harmonic bonds (stiffness 5000 eV Å<sup>-2</sup>) and a harmonic angle of 180° (stiffness 5000 eV rad<sup>-2</sup>). These values were chosen to provide a rigid SWCNT network at low temperatures, but to allow for deformation at higher temperatures. The interaction between beads on different SWCNTs are described by the 12-6 Lennard-Jones potential (length scale of 11 Å, energy scale of 1 eV). 5291 aligned SWCNTs of length 1 μm were initially placed in a 1.05 × 1.05 × 1.05 μm<sup>3</sup> simulation cell, so that the density of the model structure was 8 kg m<sup>-3</sup>, the same as that of the experimental samples. The system temperature was gradually increased from 0 to 20 000 K and then kept at a temperature of 20–000 K for 40 ns. This procedure melted the initial structure, randomly orienting the SWCNTs. The system was then cooled down to a temperature of 300 K over 10 ns and kept there for 20 ns. The final structure of the network model is shown in Figure 5. There are 20–30 junctions on each SWCNT, close to a previous estimation.<sup>[57]</sup>

**Accommodation Coefficient Simulation:** Molecular dynamics simulations were used to predict the gas-SWCNT accommodation coefficients. The structure used is shown in Figure 6 and comprises two concentric SWCNTs of 40 nm length. The outer (36, 36) and the inner (6, 6) SWCNTs have diameters of 48 Å and 8 Å.

The MD simulations were performed using LAMMPS.<sup>[59]</sup> The interactions between carbon atoms was modeled with the adaptive intermolecular reactive empirical bond-order (AIREBO) potential<sup>[60]</sup> and the interactions between carbon-gas and gas-gas were modeled with 12-6 Lennard-Jones potentials (see Supporting Information Table S1). The simulation time step was 1 fs and periodic boundary conditions were applied in all directions.

At a gas pressure of 506 kPa, the system was equilibrated to a temperature of 300 K using the Nose-Hoover thermostat within 500 ps. This high pressure reduces simulation time by tracking more gas atoms simultaneously, while remaining in the free molecular gas transport regime, as gas-gas collisions are rare relative to gas-SWCNT collisions. The global thermostat was then turned off and a heat source (or sink) (1–10 pW depending on the gas) was applied to the outer SWCNT and a heat sink (or source) of the same magnitude was applied to the inner SWCNT, both through velocity rescaling. Steady state was reached after ≈10 ns as a result of collisions between the gas molecules and the SWCNTs and data was collected for 40 ns in each simulation. For all the simulations, the temperature of the inner SWCNT was kept at 300 K and the temperature of the outer SWCNT was varied (260–340 K).

To calculate the energy accommodation coefficient, we monitored the energy of the gas atoms entering and departing a virtual cylinder of radius 13 Å surrounding the inner SWCNT. This radius is equal to the radius of the inner SWCNT plus the SWCNT-gas LJ cutoff distance. From the energy stream of gas molecules entering and departing this virtual cylinder, we calculated the energy accommodation coefficient from<sup>[50,52]</sup>

$$\alpha = \frac{E_{in} - E_{re}}{E_{in} - E_w} = \frac{\sum E_{in}(i) - \sum E_{re}(i)}{3/2 N k_B (T_{gas} - T_{CNT})} \quad (11)$$

## Supporting Information

Supporting Information is available from the Wiley Online Library or from the author.

## Acknowledgements

This work was supported by the NSF through grants CBET-0933510 (AJHM,MFI,LH,KHK) & DMR-0645596 (MFI), and by the AFOSR Young Investigator Program FA95501110030 (J.A.M., S.N.S.). The authors thank Craig Maloney, the NSF REU Summer Program (DMR-1005076), undergraduate summer research assistant David Ring, and

undergraduate Gabriella Coloyan. S.N.S. also thanks the Carnegie Mellon Steinbrenner Fellowship.

Received: May 11, 2012

Revised: July 7, 2012

Published online: August 3, 2012

- [1] A. Panetti, in *Space Mission Analysis and Design*, Microcosm Press, El Segundo, **1999**, pp. 428–458.
- [2] K. S. Udell, *Int. J. Heat Mass Transfer* **1985**, *28*, 485.
- [3] J. S. Q. Zeng, P. C. Stevens, A. J. Hunt, R. Grief, D. Lee, *Int. J. Heat Mass Transfer* **1996**, *39*, 2311.
- [4] X. Lu, M. C. Arduini-Schuster, J. Kuhn, O. Nilsson, J. Fricke, R. W. Pekala, *Science* **1992**, *255*, 971.
- [5] S. S. Kistler, A. G. Caldwell, *Ind. Eng. Chem.* **1934**, *26*, 658.
- [6] K. Ishikawa, S. Chiashi, S. Badar, T. Thurakitseree, T. Hori, R. Xiang, M. Watanabe, J. Shiomi, S. Maruyama, *Proc. ASME/JSM E Therm. Eng. Jt. Conf., 8th* **2011**, *2011*, T30061.
- [7] X. Gui, J. Wei, K. Wang, A. Cao, H. Zhu, Y. Jia, Q. Shu, D. Wu, *Adv. Mater.* **2010**, *22*, 617.
- [8] X. C. Gui, A. Y. Cao, J. Q. Wei, H. B. Li, Y. Jia, Z. Li, L. L. Fan, K. L. Wang, H. W. Zhu, D. H. Wu, *ACS Nano* **2010**, *4*, 2320.
- [9] J. Yang, S. Waltermire, Y. Chen, A. A. Zinn, T. T. Xu, D. Li, *Appl. Phys. Lett.* **2010**, *96*, 023109.
- [10] J. Hone, M. Whitney, C. Piskoti, A. Zettl, *Phys. Rev. B* **1999**, *59*, R2514.
- [11] M. Fujii, X. Zhang, H. Xie, H. Ago, K. Takahashi, T. Ikuta, H. Abe, T. Shimizu, *Phys. Rev. Lett.* **2005**, *95*, 065502.
- [12] E. Pop, D. Mann, Q. Wang, K. Goodson, H. Dai, *Nano Lett.* **2005**, *6*, 96.
- [13] C. Yu, L. Shi, Z. Yao, D. Li, A. Majumdar, *Nano Lett.* **2005**, *5*, 1842.
- [14] T.-Y. Choi, D. Poulidakos, J. Tharian, U. Sennhauser, *Nano Lett.* **2006**, *6*, 1589.
- [15] M. Schmidt, F. Schwertfeger, *J. Non-Cryst. Solids* **1998**, *225*, 364.
- [16] D. N. Futaba, K. Hata, T. Yamada, T. Hiraoka, Y. Hayamizu, Y. Kakudate, O. Tanaike, H. Hatori, M. Yumura, S. Iijima, *Nat. Mater.* **2006**, *5*, 987.
- [17] J. Biener, M. Stadermann, M. Suss, M. A. Worsley, M. M. Biener, K. A. Rose, T. F. Baumann, *Adv. Mater.* **2011**, *4*, 656.
- [18] R. R. Mitchell, B. M. Gallant, C. V. Thompson, Y. Shao-Horn, *Energy Environ. Sci.* **2011**, *4*, 2952.
- [19] V. Presser, M. Heon, Y. Gogotsi, *Adv. Funct. Mater.* **2011**, *21*, 810.
- [20] T. Bordjiba, M. Mohamedi, L. H. Dao, *Adv. Mater.* **2008**, *20*, 815.
- [21] Y. Zhai, Y. Dou, D. Zhao, P. F. Fulvio, R. T. Mayes, S. Dai, *Adv. Mater.* **2011**, *23*, 4828.
- [22] B. Assfour, S. Leoni, G. Seifert, I. A. Baburin, *Adv. Mater.* **2011**, *23*, 1237.
- [23] C. Feng, K. Liu, J.-S. Wu, L. Liu, J.-S. Cheng, Y. Zhang, Y. Sun, Q. Li, S. Fan, K. Jiang, *Adv. Funct. Mater.* **2010**, *20*, 885.
- [24] T. Umeyama, N. Tezuka, S. Seki, Y. Matano, M. Nishi, K. Hirao, H. Lehtivuori, N. V. Tkachenko, H. Lemmetyinen, Y. Nakao, S. Sakaki, H. Imahori, *Adv. Mater.* **2010**, *22*, 1767.
- [25] M. T. Pettes, H. Ji, R. S. Ruoff, L. Shi, *Nano Lett.* **2012**, *12*, 2959.
- [26] K. Ishikawa, S. Tanaka, K. Miyazaki, J. Shiomi, S. Maruyama, *2nd Int. Forum Heat Transfer*, Tokyo, Japan **2008**.
- [27] R. S. Prasher, X. J. Hu, Y. Chalopin, N. Mingo, K. Lofgreen, S. Volz, F. Cleri, P. Keblinski, *Phys. Rev. Lett.* **2009**, *102*, 105901.
- [28] A. A. Balandin, S. Ghosh, W. Z. Bao, I. Calizo, D. Teweldebrhan, F. Miao, C. N. Lau, *Nano Lett* **2008**, *8*, 902.
- [29] I. K. Hsu, M. T. Pettes, M. Aykol, L. Shi, S. B. Cronin, *J. Appl. Phys.* **2010**, *108*, 4.
- [30] I.-K. Hsu, M. T. Pettes, M. Aykol, C.-C. Chang, W.-H. Hung, J. Theiss, L. Shi, S. B. Cronin, *J. Appl. Phys.* **2011**, *110*, 044328.

- [31] M. B. Bryning, D. E. Milkie, M. F. Islam, L. A. Hough, J. M. Kikkawa, A. G. Yodh, *Adv. Mater.* **2007**, *19*, 661.
- [32] K. H. Kim, M. Vural, M. F. Islam, *Adv. Mater.* **2011**, *23*, 2865.
- [33] G. Gao, T. Çagin, W. A. Goddard III, *Nanotechnology* **1998**, *9*, 184.
- [34] S. Brunauer, P. H. Emmett, E. Teller, *J. Am. Chem. Soc.* **1938**, *60*, 309.
- [35] S. L. Brantley, N. P. Mellott, *Am. Mineral.* **2000**, *85*, 1767.
- [36] A. Peigney, C. Laurent, E. Flahaut, R. R. Bacsa, A. Rousset, *Carbon* **2001**, *39*, 507.
- [37] S. N. Schiffrès, J. A. Malen, *Rev. Sci. Instrum.* **2011**, *82*, 064903.
- [38] J. Hone, B. Batlogg, Z. Benes, A. T. Johnson, J. E. Fischer, *Science* **2000**, *289*, 1730.
- [39] S.-M. Lee, D. G. Cahill, *J. Appl. Phys.* **1997**, *81*, 2590.
- [40] M. A. Schuetz, L. R. Glicksman, *J. Cell. Plast.* **1984**, *20*, 114.
- [41] E. W. Lemmon, M. O. McLinden, D. G. Friend, in *NIST Chemistry WebBook*, Gaithersburg, <http://webbook.nist.gov/chemistry/fluid/> (accessed February 2012).
- [42] W. M. Kays, M. E. Crawford, *Convective Heat And Mass Transfer*, McGraw-Hill, New York **1980**.
- [43] R. Perkins, D. Friend, H. Roder, C. Nieto de Castro, *Int. J. Thermophys.* **1991**, *12*, 965.
- [44] S. M. Lee, K. S. Park, Y. C. Choi, Y. S. Park, J. M. Bok, D. J. Bae, K. S. Nahm, Y. G. Choi, S. C. Yu, N. Kim, T. Frauenheim, Y. H. Lee, *Synth. Met.* **2000**, *113*, 209.
- [45] S. M. Lee, Y. H. Lee, *Appl. Phys. Lett.* **2000**, *76*, 2877.
- [46] F. L. Darkrim, P. Malbrunot, G. P. Tartaglia, *Int. J. Hydrogen Energy* **2002**, *27*, 193.
- [47] B. Panella, M. Hirscher, S. Roth, *Carbon* **2005**, *43*, 2209.
- [48] Z. Chen, W. Ren, L. Gao, B. Liu, S. Pei, H.-M. Cheng, *Nat. Mater.* **2011**, *10*, 424.
- [49] Y. Fu, B. Carlberg, N. Lindahl, N. Lindvall, J. Bielecki, A. Matic, Y. Song, Z. Hu, Z. Lai, L. Ye, J. Sun, Y. Zhang, Y. Zhang, J. Liu, *Adv. Mater.* **2012**, *24*, 1576.
- [50] S. J. Jeans, *An Introduction to The Kinetic Theory of Gases*, Cambridge University Press, Cambridge **1940**.
- [51] T. K. Tokunaga, *J. Chem. Phys.* **1985**, *82*, 5298.
- [52] G. S. Springer, in *Advances in Heat Transfer* (Eds: T. Irvin, J. Hartnett), Elsevier, New York **1971**, pp. 163–218.
- [53] F. O. Goodman, *J. Phys. Chem.* **1980**, *84*, 1431.
- [54] D. E. Johnston, M. F. Islam, A. G. Yodh, A. T. Johnson, *Nat. Mater.* **2005**, *4*, 589.
- [55] M. F. Islam, E. Rojas, D. M. Bergey, A. T. Johnson, A. G. Yodh, *Nano Lett.* **2003**, *3*, 269.
- [56] S. H. Jeong, K. K. Kim, S. J. Jeong, K. H. An, S. H. Lee, Y. H. Lee, *Synth. Met.* **2007**, *157*, 570.
- [57] L. A. Hough, M. F. Islam, B. Hammouda, A. G. Yodh, P. A. Heiney, *Nano Lett.* **2006**, *6*, 313.
- [58] C. Nan, *J. Appl. Phys.* **1997**, *81*, 6692.
- [59] S. Plimpton, *J. Comput. Phys.* **1995**, *117*, 1.
- [60] S. J. Stuart, A. B. Tutein, J. A. Harrison, *J. Chem. Phys.* **2000**, *112*, 6472.